Vol. 45 — N° 3 09 21 p. 457 – 476

GEOSTANDARDS and GEOANALYTICAL RESEARCH

Exploring Biases in Atom Probe Tomography Compositional Analysis of Minerals

Chiara **Cappelli** (1)*, Sandi **Smart** (1, 2), Harold **Stowell** (1) and Alberto **Pérez-Huerta** (1)

(1) Department of Geological Sciences, The University of Alabama, Tuscaloosa, AL, 35487, USA
(2) Department of Oceanography, University of Cape Town, Rondebosch 7701, South Africa
* Corresponding author. e-mail: ccappelli@ua.edu

Atom probe tomography (APT) is emerging as a key nanogeochemistry technique for diverse geoscience applications. Estimating stoichiometric mineral compositions is particularly challenging for features at nanoscale. APT provides reliable measurements for metallic systems but the reliability for oxides is problematic, notably due to oxygen deficit. Here, we use laser-assisted APT to compare results for spinel and garnet crystals. APT compositional results were compared with those by electron microprobe to determine the possible APT analytical inaccuracy. Extensive data processing was accomplished, including correlation histograms, 2D ion distribution maps and 1D elements concentration profiles, to disclose the possible mechanisms leading to mineral stoichiometry biases. Multiple events and neutral molecules formation are probable the main processes responsible for atom deficit. In particular, the amount of the same isotope–same charge state ion pairs correlated with aluminium and oxygen deficits suggests that the co-evaporation in a dead space–dead time window could lead to a significant decrease of detected ions. Also, molecular species dissociation and direct current evaporation could partially account for further atom loss. Overall, better APT compositional estimation was obtained for spinel, which has lesser variation in lattice sites and greater overall lattice symmetry, higher thermal conductivity and lower band gap compared with garnet.

Keywords: field evaporation, laser-assisted, mineral stoichiometry, cation co-ordination, oxygen deficit.

Received 13 Jan 21 – Accepted 18 May 21

Laser-assisted field evaporation has significantly expanded the application of atom probe tomography (APT) from the exclusive study of conductors to the analysis of semiconductors and insulator materials (Gault *et al.* 2010a, Devaraj *et al.* 2017, Reddy *et al.* 2020). Among insulators, geological materials are becoming an important component of routine APT analysis (Reddy *et al.* 2020), due to a growing interest in the technique within the Earth Sciences.

Of the minerals studied so far, very good results have been documented for APT analysis of carbonates (McMurray *et al.* 2011, Felmy *et al.* 2015, Pérez-Huerta *et al.* 2016, 2019, Pérez-Huerta and Laiginhas 2018), phosphates (Gordon *et al.* 2012, 2015, Santhanagopalan *et al.* 2015, La Fontaine *et al.* 2016, Fougerouse *et al.* 2018, DeRocher *et al.* 2020), sulfate and sulfide minerals (Fougerouse *et al.* 2016, 2019, Weber *et al.* 2016, Weber *et al.* 2018, Cappelli and Pérez-Huerta 2020), oxides (Kuhlman *et al.* 2001, Gordon and Joester 2011, Genareau *et al.* 2019, Taylor *et al.* 2019, Verberne *et al.* 2019, 2020) and silicates (Arey *et al.* 2012, Bachhav *et al.* 2015, Valley *et al.* 2015, Piazolo *et al.* 2017, Exertier *et al.* 2018, Saxey *et al.* 2018, White *et al.* 2018, Bloch *et al.* 2019). The application of APT to these minerals has provided significant information for geochronology (Valley *et al.* 2014, 2015, Saxey *et al.* 2018, Verberne *et al.* 2019), biogeochemistry and biomineralisation (Gordon *et al.* 2012, Branson *et al.* 2016, La Fontaine *et al.* 2016, Pérez-Huerta *et al.* 2019, 2020), metamorphism (Peterman *et al.* 2019) and the study of extra-terrestrial materials (Heck *et al.* 2014, Daly *et al.* 2020, Lewis *et al.* 2020).

Several studies, however, have shown variability in inferred stoichiometry, frequently related to the 'loss' of oxygen during APT mineral composition analysis (Bachhav *et al.* 2011a, 2013, Weber *et al.* 2016, La Fontaine *et al.* 2017, Cappelli and Pérez-Huerta 2020). In fact, the achievement of a reliable quantitative estimate of material

doi: 10.1111/ggr.12395

composition by APT is still an important issue, not just for geological samples, but also for other insulator materials and semiconductors. The discrepancy from the materials' nominal composition is related to both the technique (analysis conditions) and the crystallographic structure and type of the analysed material (Saxey 2011, Karahka and Kreuzer 2015, Reddy *et al.* 2020). For minerals in particular, the co-ordination of cations in their structure has been proven to be a fundamental factor influencing evaporation field (Xia *et al.* 2015, Karahka and Kreuzer 2018). This is consistent with the crystal field theory that predicts that a transition metal in a specific crystal configuration (type of co-ordination polyhedron) achieves a specific crystal field stabilisation energy (CFSE) and symmetry of the co-ordination environment, depending also on the ligand nature (e.g., oxygen) (Burns 1993). Furthermore, the types of ions and their geometric arrangement in the crystal lattice are what eventually determines the thermal, electrical and optical properties of minerals and, hence, the kind of interaction between the applied voltage and laser pulse and the studied mineral during APT analysis.

In the present study, we provide a detailed APT analysis of two minerals to investigate the problems of atoms loss and inaccurate stoichiometric estimates. Specifically, we address the matter of oxygen quantification, as well as issues related to uneven ion desorption and variation in charge state ratios. A comparison is made between a natural spinel, an oxide with high symmetric transition metals co-ordination environment, and a natural garnet, a silicate with heterogeneous composition and more complex crystallographic structure. A theoretical section is also included to frame the physical principles on which the laser-mode atom probe is based and to describe the properties of the two studied materials. This theoretical background together with the obtained APT data helps in achieving the main purpose of this work, which is to better understand how mineral properties and crystallographic structure can influence the atom probe field evaporation process and lead to a divergence between the measured and the true mineral stoichiometry.

Experimental procedures

Materials

This study utilises a single spinel crystal of millimetric size (Catalogue No. 112922) provided by the American Museum of Natural History, New York, USA, and a single garnet crystal from the GNS Science PETLAB collection, Dunedin, NZ. The crystals were analysed by electron probe microanalyser (JEOL 8600 EPMA housed in the Alabama Analytical Research Center (AARC) of the University of Alabama), yielding the following structural formula:

spinel $Mg_{0.906}Ti_{0.002}V_{0.006}Cr_{0.014}Al_{2.039}O_4$
garnet $Fe_{1.642}Mn_{0.061}Mg_{0.879}Ca_{0.522}Al_{1.972}Ti_{0.007}Si_{2.962}O_{12}$

The spinel has very low contents of transition elements (Ti, V, Cr) in the general formula: XAl_2O_4. On the other hand, the aluminium garnet is characterised by the four components solid solution (Mg, Fe, Mn and Ca) and possible substitution of Fe (III) for Al in the general structural formula: $X_3Y_2Z_3O_{12}$. Note that APT garnet sample was extracted from the core of the crystal to avoid compositionally zoned rims and EPMA measurements were performed in the same area (in the range of 50 μm).

APT specimen preparation

The specimens for atom probe analysis were prepared following a conventional focused ion beam (FIB) protocol (Miller *et al.* 2007, Gault *et al.* 2012a, Larson *et al.* 2013, Miller and Forbes 2014), using a dual beam scanning electron microscope (TESCAN LYRA FIB-FESEM) (the description of the protocol is reported in online supporting information). A sample coating of ~20 nm of gold was performed before the FIB milling in order to minimise surface charging effects. The final tip-shaped specimens had a radius of curvature (half diameter of the top of the tip) ranging from 16 to 47 nm and shank angles between 9° and 48° (Figure S1). Note that because the sample stage is tilted during tip sharpening, radius and shank angles were measured applying a 35° geometric correction, which gives reliable SEM tip's images. Spinel and garnet behave differently during FIB milling, being the first more prone to form sharp tips (small shank angles).

Local electrode atom probe runs and data analysis

Six specimens for each mineral were analysed in laser mode (laser wavelength of 355 nm) by a local electrode atom probe (LEAP 5000 XS, housed at the AARC of The University of Alabama) with a nominal flight path of 100 mm. Two values of the laser pulse energy (LE) (30 and 50 pJ) were used, while the detection rate and the laser pulse rate were fixed at constant values (0.5% and 125 kHz respectively). The direct current (DC) voltage varied freely in order to maintain a stable detection rate. Successful APT results were obtained for all six of the garnet specimens (three at each laser energy), but for only four of the spinel specimens (three at 30 pJ and one at 50 pJ) due to early

fracture of the remaining two tips at the higher laser energy setting (Tables S1 and S2).

Integrated Visualisation and Analysis Software (IVAS 3.8.0) from CAMECA was used for the spectra and 2D and 3D reconstructions of the data sets, while files in EPOS format were used for multihit correlation histograms (Saxey plots) and ion dissociation work with MATLAB R2020a. A full list of instrument settings, acquisition conditions and reconstruction parameters are given in Tables S1 and S2.

Ion species: On the basis of the recorded mass-to-charge state ratios and taking into account EPMA bulk analysis, ions species were defined for each peak of the APT spectra. The peak range was fixed to a width of 0.1 Da for the lower bound and 0.2 Da for the upper bound to account for possible peak tails. When bigger tails were observed, the ranges were manually broadened for a correct ion counting. We believe that this approach is the best in the context of this study since it may lead to slight overestimates of minor isotopic species and trace elements concentration but without significantly influencing bulk compositional estimates.

The local background estimate was based on the local range-assisted model, which applies as default when IVAS peak decomposition analysis is performed, as the case of the present study. The resolution is reported in Tables S1 and S2 as mass resolution ($M/\Delta M$) where M stands for the mass of the highest peak in the spectrum (Mg^{2+} for spinel and O^+ for garnet) and ΔM for the full width at either half or tenth maximum. Overlap of contiguous peaks was resolved when possible by the decomposition tool, which allows the estimation of the distribution of ion counts between different species considering the relative concentrations of ion isotopes.

On the other hand, singly charged monoatomic and doubly charged diatomic species, which share the same peak of the APT spectrum, are not distinguishable. The case of the oxygen is particularly problematic since the post-ionisation of O_2^+ is likely to occur. However, previous experimental studies performed on ^{18}O-enriched oxides (Bachhav *et al.* 2013, Kinno *et al.* 2014) and results of theoretical studies modelling molecular cluster field evaporation (e.g., Karahka and Kreuzer 2013) demonstrate that the dominant ion species forming during oxides APT analysis is O^+. It is also worth noting that O_2^{2+} is a metastable molecule, most likely derived, as above mentioned, from O_2^+ post-ionisation, and its formation, as documented for O_2 electron spectroscopy analysis (Sigaud *et al.* 2013, Song *et al.* 2019), may compete with different dissociation processes of the parent species (e.g., pathways 1. $O^+ + O^0$ and 2. $O^+ + O^+$).

Given these recent evidences, the peak at 16 Da was only assigned to $^{16}O^+$. Nevertheless, to validate this choice, different scenarios where a percentage of the peak counts was assigned to O_2^{2+} were considered and discussed (see Discussion section).

Theoretical background

Ion field evaporation from insulators and the non-stoichiometry problem: While experimental evidence corroborates the effectiveness of laser pulse in inducing field evaporation of ions from metals, semiconductors and insulators, the mechanism triggering the departure of atoms from the APT tip-shaped specimen surface is still a topic of debate. In fact, the field evaporation process is not yet fully understood and an exhaustive quantomechanic description of the phenomenon is difficult to achieve (Karahka and Kreuzer 2013). The general theory considers the existence of an energy barrier $Q_{EV}(F)$ that atoms must overcome in order to desorb from the surface. This process is temperature- and field-dependent, and the equation describing the atom desorption rate $k_{EV}(F,T)$ can be written as:

$$k_{EV}(F, T) = A e^{-\left(\frac{Q_{EV}(F)}{k_B T}\right)} \quad (1)$$

where A is the pre-exponential factor, k_B the Boltzmann constant and T the specimen temperature. The energy barrier is inversely proportional to the electric field (F) and it reaches a zero value for a threshold electric field F_{EV} that corresponds to the atom evaporation field. Desorbed atoms are immediately fully ionised because of the intense field. The magnitude of the electric field would depend on the applied voltage (V_{DC} where DC stands for direct current) and the tip-shaped specimen radius (R) according to the equation:

$$F = \frac{V_{DC}}{kR} \quad (2)$$

where k is the field factor, a dimensionless parameter related to the specimen shape and the electrostatic environment (Lefebvre-Ulrikson *et al.* 2016) that accounts for the reduction of the specimen electric field with respect to the field of a theoretical charged sphere with the same radius of curvature (Gault *et al.* 2010a). The focus of this section is to *qualitatively* describe the theoretical interaction between a laser and an insulator material immerged in a high electric field to evaluate the potential biasing effect of the APT laser pulse on the estimation of a given mineral composition. For

further information on the equations modelling the process of atom field evaporation, we remit to previous extensive literature (Gault *et al.* 2012b, Larson *et al.* 2013, Vurpillot and Oberdorfer 2015, Vurpillot 2016).

The use of a laser pulse introduces a new variable to the specimen electric field space system normally encountered in APT voltage mode. On the basis of the existing theories, it is likely that the laser pulse promotes a thermal pulsing mechanism within the sample (Vurpillot *et al.* 2009, Gault *et al.* 2010b, Vella *et al.* 2011, Müller *et al.* 2012, Kelly *et al.* 2014, Valderrama *et al.* 2015), coupled with an alteration of the surface electronic structure (Silaeva *et al.* 2014). The theoretical principle is that, in a high electric field, besides physical processes (i.e., molecule polarisation), chemical processes alter the base electronic configuration of the molecules in the tip-shaped APT specimen, possibly establishing new bonding orbitals (Silaeva *et al.* 2013). In agreement with the thermal pulse model, the laser pulse generates carriers (i.e., free electrons and holes) whose energy transfer would be mediated by *hot* phonons (Cerezo *et al.* 2006, Vurpillot *et al.* 2009, Silaeva *et al.* 2015) that lead to a fast heating of the tip apex through a thermalisation process (Kelly *et al.* 2014). This mechanism may be enabled by the high applied electric field, which induces a decrease in the high HOMO-LUMO gap (bulk band bending) of semiconductors and insulators (Silaeva *et al.* 2013, Karahka and Kreuzer 2015), enhancing the laser absorption up to values typical for metals (Silaeva *et al.* 2014).

Hence, non-metallic minerals must undergo a process of 'metallisation' (Silaeva *et al.* 2014) in order to be field-evaporated during APT analysis and the extent of this process depends on the nature of the mineral. From a macroscopic point of view, parameters such as thermal conductivity and diffusivity and band gap energies can be linked to the effectiveness of the field evaporation and thus to the variation of the mineral composition estimates with the applied voltage and laser energy (Bachhav *et al.* 2011b, Valderrama *et al.* 2015). At a molecular level, the co-ordination and nature of the atoms at the specimen surface is what determines the changes in the chemical and physical properties of a mineral under the influence of an applied voltage and a laser pulse and that eventually leads to local evaporation patterns (Gault *et al.* 2010a).

Quantomechanic studies have demonstrated through cluster models that the evaporation field strength is a function of the binding sites, such that where weaker binding exists (e.g., single atoms on flat surfaces (adatoms), kinks, ledge adatoms), the local field enhances (Karahka and Kreuzer 2015, Karahka and Kreuzer 2018). Moreover, in their study on the kinetics of Si field evaporation, Karahka and Kreuzer (2018) have observed a significant difference between the field evaporation of single-co-ordinated and multiple co-ordinated sites reporting higher fields for multiple bonds. In fact, it has already been demonstrated for semiconductors, oxides and some minerals how local and bulk stoichiometry can vary as a function of the electric field and how in turn the surface field distribution correlates with the sample crystallographic directions (Riley *et al.* 2012, Diercks *et al.* 2013, Mancini *et al.* 2014, Morris *et al.* 2019, Cappelli and Pérez-Huerta 2020). From the above considerations, it is evident that the influence of the mineral crystallography (i.e., lattice structure and symmetry, atom co-ordination) and composition on APT analysis can be significant, in addition to the laser energy and the applied voltage.

Crystallographic structure and cation co-ordination in spinel and garnet: Figure 1 shows a simplified illustration of the crystallographic structure of spinel (isometric, hexoctahedral, octahedron morphology) and garnet (isometric, hexoctahedral, dodecahedron morphology). Despite the two minerals belonging to the same crystallographic system (i.e., isometric), the different co-ordination of their elements is immediately apparent. Chains of edge-shared octahedra linked by isolated tetrahedra describe the three-dimensional spinel structure (Figure 1, left). In garnet, eightfold co-ordinated metal sites share edges with octahedra and tetrahedra (Figure 1, right). Moreover, it is important to note that different elements occupy similar crystallographic sites in the two minerals. For example, while divalent Mg occupies tetrahedra sites in spinel, tetravalent Si forms strong bonds with oxygens in garnet tetrahedra. Both atom co-ordination and mineral composition lead to different physicochemical properties for the two minerals that ultimately elicit distinct behaviour when laser pulse and high field are applied to a needle-shaped specimen during APT analysis. For the thermal properties of spinel and garnet relevant to the thermal assisted field evaporation process, refer to Table 1.

Results

Atom probe tomography combines the compositional estimation of a material with its representation in 2 and 3D space. Hence, data processing includes (a) ion count analysis and (b) spatial reconstruction. For the former, peak ranging of the spectra is the primary operation to be done, but other useful aspects can be investigated to better understand the behaviour of the material exposed

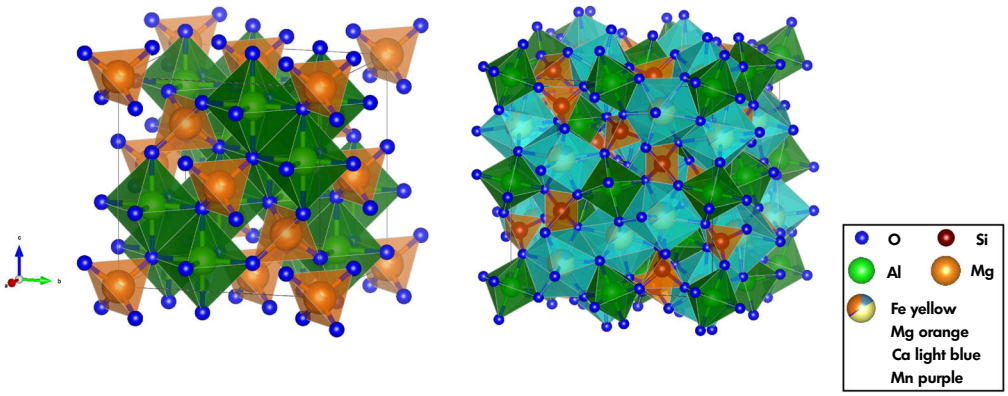

Figure 1. Schematic of atom arrangement and polyhedra in the spinel (left) and garnet (right) crystal lattice. Polyhedra design: [AlO_6] octahedra (green); [MgO_4] (in spinel) and [SiO_4] (in garnet) tetrahedra (orange); eightfold co-ordinated Mg, Ca and transition metal sites (light blue polyhedra in garnet). See legend for the atom colour designation.

Table 1.
Garnet and spinel electronic band gap and thermal properties

	Heat capacity (Jg^{-1} K^{-1})	Thermal conductivity (Wm^{-1} K^{-1})	Thermal diffusivity (m^2 s^{-1}) × 10^{-6}	Band gap (eV)
Spinel[a]	0.82	16.2	5.56	
Spinel[b]				7.8
Garnet-1[c]	0.74	3.31	1.14	
Garnet-2[c]	0.74	3.14	1.09	
Garnet[d]				8.2

[a] 295 K, Harris *et al.* (2013).
[b] Shengli *et al.* (2012).
[c] 298 K, garnet-1 Py41Al46Gr13, garnet-2 Py40Al46Gr14, where Py (pyrope), Al (almandine), Gr (grossular) and the number stands for %, Giesting and Hofmeister (2002).
[d] Nitsan and Shankland (1976).

to high electric field and laser pulse and, in turn, to better interpret the obtained data. The study of multihit events, for example, provides insights on the possible reasons of ion count deficit and potentially allows the recovering of part of non-detected counts. The charge state ratio (CSR) is another measurable factor that gives valuable information about the surface distribution of the electric field, which is the parameter that eventually determines the atom evaporation and ionisation. In the same way, 2D maps together with the 3D reconstructions are useful to visualise the atom spatial distribution, complement the CSR measurements and give illustrative description of the sample–laser interaction. The above-mentioned data processes are described in the following sections for spinel and garnet APT data.

Spectra and 3D reconstructions

APT mass-to-charge state ratio spectra of spinel and garnet show several molecular species (composed of oxygen and metals) and multiple charge states for the main elements and molecules (Figure 2). For both minerals, no significant difference was found between the spectra obtained at 30 pJ versus 50 pJ in terms of ranged ion species, low background was registered, and a quite good resolution was obtained in all cases (see mass resolution values at full width at half maximum ($M/\Delta M$) and full width at one-tenth ($M/\Delta M_{10}$) in Tables S1 and S2). However, for spinel, large thermal tails characterise the spectrum at 50 pJ laser energy, which, in practice, lowers the resolution. Also, despite the good mass resolution the overlapping of some peaks (e.g., Si^+ and Fe^{2+} for garnet) adds in general a level of complexity to the determination of the species ranges and, ultimately, of the count distribution.

The tip reconstruction parameters were fixed to default values which fall in the general ranges used for the point-projection reconstruction (k factor between 2 and 8; image compression factor between 1 and 2) (Gault *et al.* 2008) (Tables S1 and S2), and shank evolution mode was chosen for the tip radius determination during the run as a suitable method for non-constant field evaporation materials. Since the 3D tip reconstructions show a fairly homogeneous atom distribution for both spinel and garnet (Figure S2), and considering the lack of specific elements that could guide a more accurate reconstruction (e.g., clear crystallographic directions (poles), clusters, secondary phases), no further

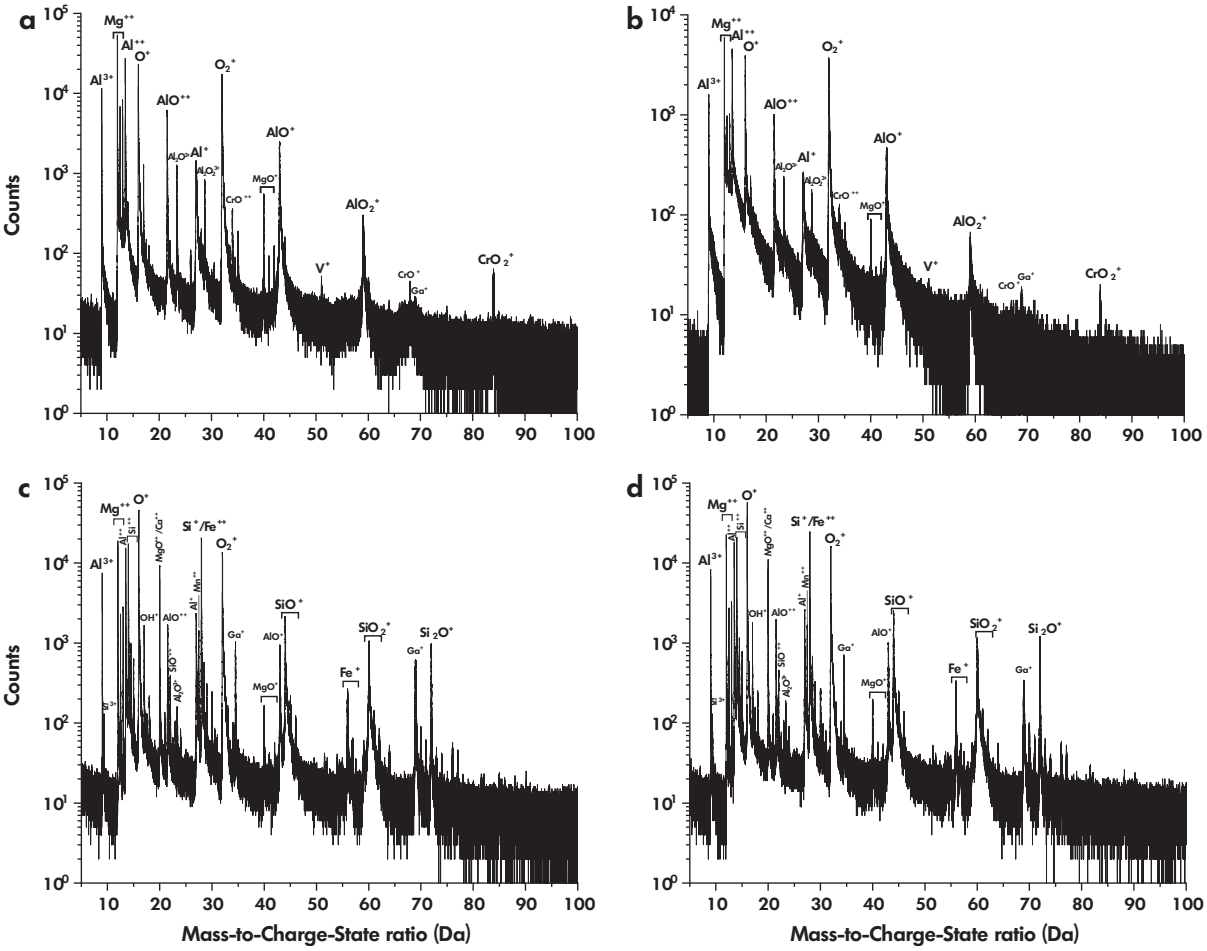

Figure 2. Spectra of representative specimens of spinel (a, b) and garnet (c, d) analysed at 30 pJ (a, c) and 50 pJ (b, d) laser energy.

testing of the reconstruction parameters was performed. Notably, some tip specimens were particularly affected by Ga contamination during FIB preparation. This can occur when low kV cleaning (5 kV) is too short and the previous sharpening phase (30 kV) has induced Ga implantation. For two spinel specimens (04123-M16 and 04184-M19), the Ga was found to be associated with a higher concentration of OH that in the case of specimen 04184-M19 (run at 50 pJ laser energy) accumulated along a microfracture. For this reason, the estimated mineral composition was based on an uncontaminated region of interest (ROI) of the tip volume (see Figure S3). The OH peak of the new ROI was considered part of the sample.

Stoichiometry from APT vs. EPMA

Element concentration estimated by APT was compared with EPMA data (note that atomic per cent (at%) was recalculated after subtracting Ga counts from the total count) (Tables 2 and 3). For spinel, a depletion in oxygen (2.4–4.1 at%), an excess of Mg (3–4.8 at%) and a slight deficit of Al (~ 1 at%) were recorded for laser pulse energy 30 pJ and detection rate 0.5%. At laser energy 50 pJ and detection rate 0.5% (specimen 04184-M19; Table 2), the oxygen percentage almost matches the EPMA stoichiometric value although Mg remains in excess (~ 1.9 at%) and a higher deficit of Al was found (~ 2.2 at%). The observed excess of Ti and Cr could be due to the overlapping of peaks in the 32–34 Da range (TiO^{2+}, CrO^{2+}), which may be leading to an overestimation of these elements and consequently to a slight underestimation of oxygen during the decomposition operation of the IVAS software. It is also worth noting that a small amount of Si was recorded by APT, while it was undetected by EPMA. Two peaks, at 14 and 28 Da, were assigned to Si. The appearance of the isotopes at 29 and 30 mass-to-charge ratios confirmed the presence of silicon and, at the same time, prevented the quantification of the small amount of iron. The low Mn

Table 2.
Elemental composition (in at%) of spinel specimens obtained from EPMA (left) and APT (right)

Element	EPMA	APT at LE 30pJ				APT at LE 50pJ
		04121-M13	04122-M15	04123-M16	03770-DR1[a]	04184-M19
O	57.40%	55.02%	53.33%	53.43%	50.50%	56.97%
Cr	0.21%	0.35%	0.27%	0.27%	0.31%	0.41%
Mg	13.00%	16.06%	17.82%	17.54%	18.63%	14.92%
Al	29.26%	28.28%	28.15%	28.32%	29.94%	27.14%
Ti	0.02%	0.20%	0.16%	0.08%	0.40%	0.28%
V	0.09%	0.03%	0.02%	0.02%	0.02%	0.05%
Fe/Si	<0.01%	0.06%	0.26%	0.34%	0.20%	0.24%
Mn	<0.01%	–	–	–	–	–

[a] Re-calculation of APT data for specimen 03770-DR1, previously published in Cappelli and Pérez-Huerta (2020). The specimen was run at 30 pJ with a detection rate of 1%.

concentration measured by EPMA was not detected by APT.

Applying our improved ion ranging scheme (informed by EPMA) to a previously analysed spinel specimen at 30 pJ and 1% detection rate (Cappelli and Pérez-Huerta 2020), similar results to the spinel specimens analysed in this study were obtained. The atomic percentages show a significant deficit of oxygen and an excess of Mg similar to the specimens run at the same laser pulse energy in this study, but a small excess of Al was instead observed.

For the garnet general composition, in order to compare APT data with EPMA results, we did not consider trace and rare earth elements that only account for less than 0.4% of the total counts. Regardless of the pulse energy used, the APT results for garnet are the same within the standard deviation (Table 3). In general, a significant deficit of oxygen was found and, consequently, all the cations appear in excess relative to the EPMA values. The relative concentrations inferred for Si and Fe depend on the accuracy of the decomposition of the peak overlapping, given that Si^{+} and Fe^{2+} share the same main peak at 28 mass-to-charge ratio. Also, the variability of Ti concentration in spinel (Table 2) is ascribed to the overlapping of its main peaks with other species peaks (e.g., O_2^{+}matches TiO^{2+}) and the absence of its isotope peaks; hence, similarly to garnet analysis, the total concentration could be misestimated during the implementation of the decomposition tool.

Because the concentration of an ionic species in APT analysis is given as atomic percentage, the apparent abundance of one mineral element can be biased by losses of another element (e.g., oxygen). Therefore, in order to correct for this effect on our element ratio estimates and to provide a fair comparison with EPMA-derived compositions, we normalise the APT data by one (or a combination) of the main elements in a specimen, namely Al, Mg or O for spinel and Al, Mg or Si+Fe for garnet (note that oxygen was not considered for garnet given its apparent high loss). By assuming 'stoichiometric detachment' (no loss) of a particular element from the tip, we can recalculate the expected abundance of the other elements to ascertain their deficit or excess, using the following equation:

Table 3.
Elemental composition (in at%) of garnet specimens obtained from EPMA (left) and APT (right)

Element	EPMA	APT at LE 30pJ			APT at LE 50pJ		
		04187-M1	04188-M2	04190-M4	04189-M3	04191-M5	04199-M7
O	60.04%	52.02%	51.47%	51.63%	51.34%	51.40%	51.81%
Mg	3.62%	6.19%	6.21%	6.20%	6.27%	6.19%	6.23%
Al	10.08%	11.30%	11.71%	11.64%	11.50%	11.51%	11.38%
Si	15.01%	15.10%	15.12%	15.77%	15.32%	15.59%	14.42%
Ca	2.83%	3.57%	3.54%	3.40%	3.58%	3.56%	3.48%
Mn	0.30%	0.69%	0.67%	0.66%	0.68%	0.70%	0.67%
Fe	8.11%	11.11%	11.26%	10.67%	11.28%	11.01%	11.97%
Ti	0.02%	0.02%	0.02%	0.03%	0.03%	0.04%	0.04%

$$N_{M_y,\text{expected}} = N_{M_x,\text{APT}} \times \frac{M_{y,\text{EMPA}}}{M_{x,\text{EMPA}}} \quad (3)$$

where M_x is the element that is assumed to detach stoichiometrically (i.e., the normalising element), M_y is one of the other main elements of the mineral structure and N stands for the atom counts either measured by APT or expected ($N_{M_y,\text{expected}}$), that is recalculated on the basis of M_x element counts ($N_{M_x,\text{APT}}$) and the stoichiometric ratio measured by EPMA ($M_{y,\text{EMPA}}/M_{x,\text{EMPA}}$). The value of the element M_y in the mineral APT-derived structural formula ($M_{y,\text{APT}}$) was calculated by the equation:

$$M_{y,\text{APT}} = \frac{N_{M_y,\text{APT}} \times M_{y,\text{EMPA}}}{N_{M_y,\text{expected}}} \quad (4)$$

The normalised APT-derived mineral stoichiometry, for a given normalising element, is obtained by applying Equations (3) and (4) to each element of the mineral (Tables 4 and 5). For both minerals, a slight excess of magnesium was found (with the obvious exception of the Mg normalisation), the size of which depends on the laser energy used and the normalising cation. Only for spinel, at laser energy 50 pJ and normalising by oxygen, is the estimated composition very close to that measured by EPMA.

Although an exact estimation of oxygen and cations deficit from the Mg normalisation is difficult to extrapolate, the apparent magnesium excess found for all the other normalisations suggests that a loss of O and also Al, Si and/or Fe must occur during APT analysis of spinel and garnet.

Multihit analyses

Field evaporation is a probabilistic event that involves all atoms on a tip surface, meaning that, at a given laser (or voltage) pulse, one or more atoms can achieve the right conditions to evaporate (Peng *et al.* 2018). In the present study, correlation plots (Saxey plots, (Saxey 2011)) of multihit ions pairs were used to study the occurrence of multiple evaporation events (Figure 3). Only evaporation events of two detected ions following a single pulse were reconstructed, given that higher order evaporation events could decrease the signal-to-noise ratio (Santhanagopalan *et al.* 2015). Horizontal and vertical lines are apparent. The intersections of these lines devise the co-evaporated ion pairs composed of two ions of the main species. Here, for example, mono-, di- and tri-valent Al, Mg and Si ions (for garnet) correlate between them and with oxygen (O^+ and O_2^+) and/or with molecular ions such as $AlO^{+/2+}$, $SiO^{+/2+}$, SiO_2^+ and MgO^{2+}. The events along these lines arise from the field evaporation of an *i*-type ion at pulse time (t_0) followed by the evaporation of the paired *j* ion at time $t_0 + dt$ (delayed ion) and, if the delay is not significant, they will appear as tails of the main peaks of APT spectra (Saxey 2011, Peng *et al.* 2018). Similarly, numerous visible diagonal trails represent the simultaneous evaporation of the paired ions after the laser pulse (i.e., both ions are delayed). These features correspond to overlapping tails of mass-to-charge peaks in APT spectra (Saxey 2011) and can also contribute to the background. Finally, molecular ion dissociation tracks, representing the dissociation of evaporated unstable molecules, are featured by the curve-shaped lines that join the parent ions, on the diagonal line of the histograms ($m1 = m2$), with the products of their decomposition (daughters, m_{d1} and m_{d2}). The main reaction pathways associated with the dissociation tracks observed at both 30 and 50 pJ laser energy (Figure 3a, b) were identified as follows:

Table 4.
Estimation of the stoichiometry of representative spinel specimens after normalising by one of the main mineral elements (Al, Mg and O)

Element		Al normalisation		Mg normalisation		O normalisation	
	EPMA	LE30	LE50	LE30	LE50	LE30	LE50
O	4.00	3.85	4.28	2.76	3.46	*4.00*	*4.00*
Cr	0.01	0.02	0.03	0.01	0.03	0.02	0.03
Mg	0.91	1.26	1.12	*0.91*	*0.91*	1.43	1.05
Al	2.04	*2.04*	*2.04*	1.46	1.65	2.19	1.91
Ti	2.0E-03	6.0E-03	2.1E-02	4.0E-03	1.7E-02	6.0E-03	1.9E-02
V	6.0E-03	2.0E-03	4.0E-03	1.0E-03	3.0E-03	2.0E-03	3.0E-03
Fe/Si	2.0E-04	2.4E-02	1.8E-02	1.8E-02	1.4E-02	2.8E-02	1.7E-02
Mn	1.0E-04	–	–	–	–	–	–

Values in italics are adopted as equal to EPMA values for the normalising element.

Table 5.
Estimation of the stoichiometry of representative garnet specimens after normalising by one or a combination of the main mineral elements (Al, Mg and Si+Fe)

Element		Al normalisation		Mg normalisation		Si+Fe normalisation	
	EPMA	LE30	LE50	LE30	LE50	LE30	LE50
O	12.00	9.27	9.17	6.08	6.01	9.17	9.07
Mg	0.72	1.10	1.10	*0.72*	*0.72*	1.09	1.09
Al	2.01	*2.01*	*2.01*	1.32	1.32	1.99	1.99
Si	3.00	2.69	2.55	1.77	1.67	–	–
Ca	0.57	0.64	0.62	0.42	0.40	0.63	0.61
Mn	0.06	0.12	0.12	0.08	0.08	0.12	0.12
Fe	1.62	1.98	2.12	1.30	1.39	–	–
Ti	4.0E-03	4.0E-03	7.0E-03	3.0E-03	3.0E-03	4.0E-03	7.0E-03
Si+Fe	4.62	4.67	4.67	3.06	3.06	*4.62*	*4.62*

Values in italics are adopted as equal to EPMA values for the normalising element.

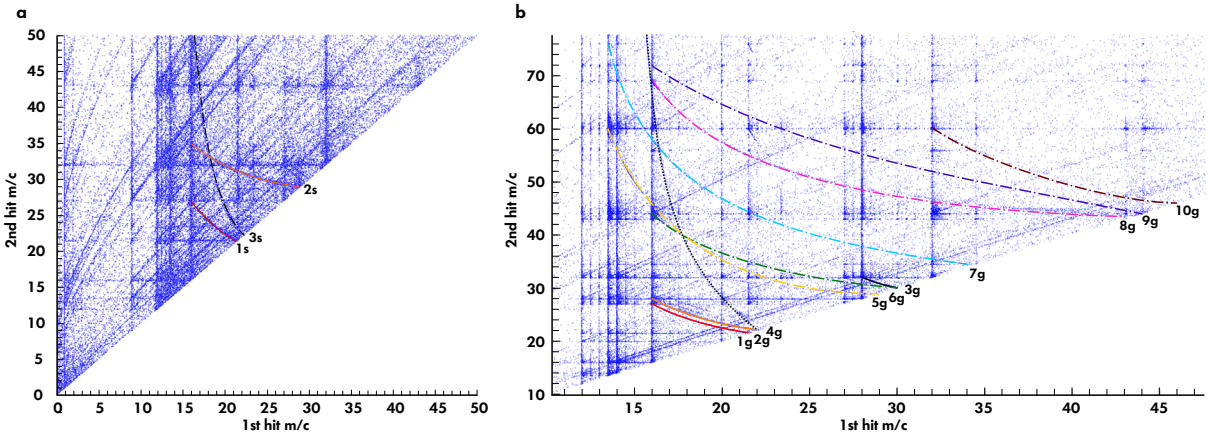

Figure 3. Mass-to-charge ratio correlation histograms of (a) spinel and (b) garnet tips analysed at 30 pJ laser pulse energy. Dissociation tracks are marked with coloured lines and the reference of the identified pathway (see text for explanation).

spinel dissociation pathways

$$1s)\ AlO^{2+} \rightarrow Al^{+} + O^{+}$$
$$2s)\ Al_2O_2^{3+} \rightarrow Al_2O^{2+} + O^{+}$$

garnet dissociation pathways

$$1g)\ AlO^{2+} \rightarrow Al^{+} + O^{+}$$
$$2g)\ SiO^{2+} \rightarrow Si^{+} + O^{+}$$
$$3g)\ SiO_2^{2+} \rightarrow Si^{+} + O_2^{+}$$

In addition, a faded, not immediate interpretable dissociation track (3s, Figure 3a) is apparent in the spinel Saxey plot. Although it is very difficult to define the entire trajectory of this track and unequivocally determine its pathway, a possible reaction is the following:

$$3s)\ CrO^{+} \rightarrow Cr^{+} + O^{+}$$

In the case of garnet, in addition to the main dissociation tracks described by Equations (1–3g), many other faint trails are visible (Figure 3b). Possible dissociation pathways describing these trails are shown in the online supporting information. For the original Saxey plots of representative specimens, we also remit to the online supporting information (Figures S4 and S5).

2D ion intensity maps

2D ion density/concentration plots are useful data reconstruction tools for recognising asymmetrical laser adsorption. Figures 4 and 5 show the 2D ion density maps of atomic and molecular species for one representative spinel and garnet tip, respectively. Immediately apparent is the higher uniformity of the spinel (Figure 4) compared with garnet maps, which show high ion density on the laser-illuminated side (white arrow, Figure 5). This ion density pattern was observed for all garnet specimens except for specimen 04199-M7, which shows a more uniform distribution for some of the main ionic species (Figures S6 and S7). This specimen has the smallest radius (27 nm) and lowest shank angle (39°) among the garnet samples.

Interestingly, features associated with low order crystallographic planes (pole and line regions) were observed for spinel at both laser energies, in agreement with Cappelli and Pérez-Huerta (2020) who performed APT analysis on spinel using 30 pJ laser energy and 1% detection rate. However, clear pole and lines are especially apparent at higher laser energy (Figure 4). In fact, the MgO 2D density plot of a specimen analysed at 30 pJ shows several spots of low ion density and a more irregular pattern. It is worth noting that the slightly more depleted area on the upper left side of the 2D plots of the 50 pJ specimen (04184-M19) could be attributed to the specimen microfracture at 70 nm depth (Figure 4). Nevertheless, because the entire area affected by the microfracture was excluded from the reconstruction of the new ROI (see 'Theoretical background' section and Figure S3), the estimated composition of the spinel specimen analysed at 50 pJ laser energy is considered reliable.

Finally, the laser effect on the ion density gradient in the *x-y* plane in general decreases along the tip length (Figures S8–S10), especially for spinel, pointing to an improvement of

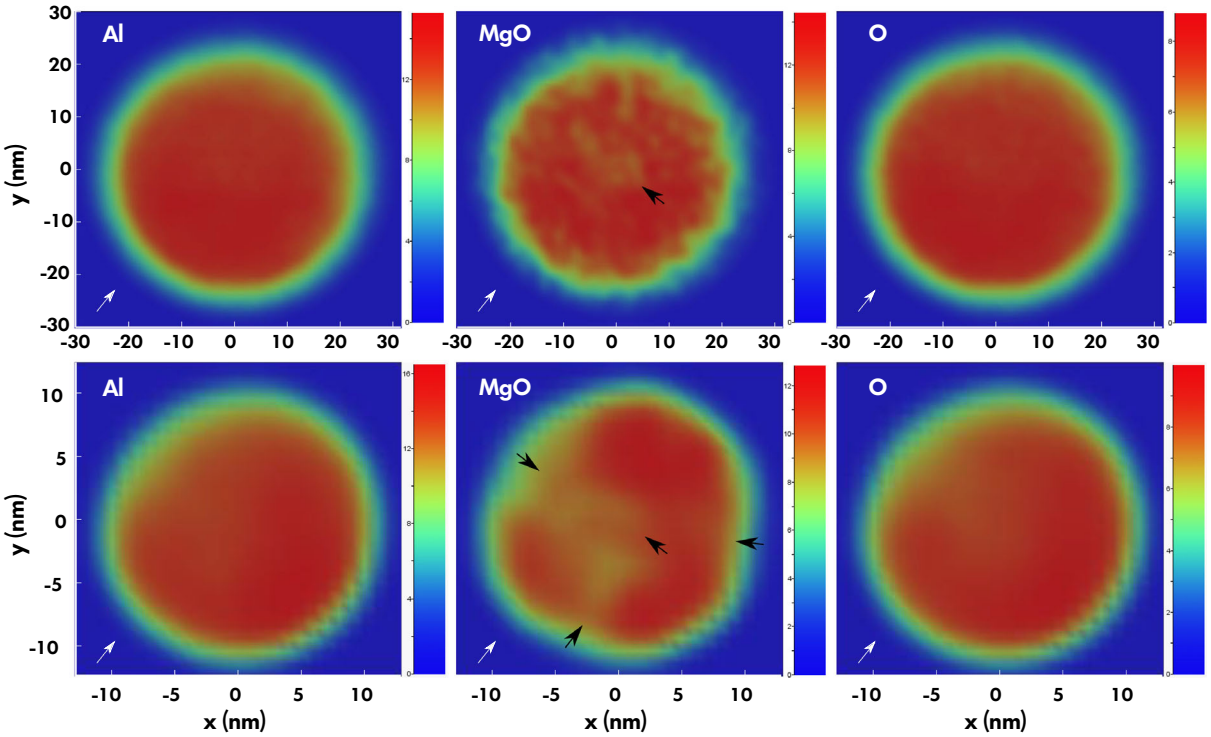

Figure 4. 2D ion density plots of a spinel specimen analysed at 30 pJ (upper maps) and 50 pJ (lower maps) laser pulse energy (white and black arrows indicate, respectively, laser beam direction and line and pole areas). Note that the spot at the top left of the 50 pJ maps is likely due to the specimen fracture at ~70 nm although a ROI was selected up to this tip depth for the plots.

the laser absorption efficiency and/or heat dissipation as the applied voltage and tip radius increase.

Charge state ratios

According to the post-ionisation theory (Kingham 1982), a relationship exists between the surface electric field of an APT specimen and the relative amount of different ion charge states (Gault *et al.* 2010a). Figure 6 shows 2D maps of ratios of single and double charged Al and Al-Si for spinel and garnet, respectively, integrated over the tip length of representative specimens. The charge state ratio (CSR) distribution of spinel varies with the laser energy, and it appears more heterogeneous at 50 pJ. At 30 pJ laser energy, a gradient following the laser direction exists although it would attenuate along the *z* axis (see Figure S8). For garnet, CSR patterns are similar among the specimens analysed, with a slight gradient in silicon CSR from the laser-illuminated side. It is important to note that, despite the IVAS decomposition tool allowing count distribution between species, the peak overlapping cannot be resolved for 2D and 3D reconstructions, as in the case of Si^{+} and Fe^{2+}. Since the peak at 28 Da was selected as Si^{+}, its concentration was overestimated in the 2D plots. Hence, the CSR values in the Si map are not accurate (CSR ~ 0.6–0.85, see colour scale in Figure 6). In fact, the reported second ionisation energies for Al (18.8 eV) and Si (16.3 eV) (Gault *et al.* 2012b) are similar, so one would expect a higher Si^{2+}/Si^{+} ratio range. Indeed, the same ratio calculated from the species abundance estimated by the count's decomposition tool ranged from an average of 2.9–6, with the higher value associated with specimen 04199-M7 which has a smaller radius and lower shank angle.

1D profiles of CSR for spinel and garnet (Figures 7 and 8) reveal a general decrease in the cation charge state ratios with increasing tip depth reflecting a decrease of the electric field as the analysis proceeds. In contrast, the oxygen ion fraction (O – IF), defined as $O^{+}/(O^{+}+O_2^{+})$, either slightly increases (as in garnet and spinel at 30 pJ) or remains constant (spinel at 50 pJ) as tip depth increases. The Al^{2+}/Al^{+} and Si^{2+}/Si^{+} ratios also increase with higher laser energy for both minerals (although the same caveat applies to the artificially low CSR values for Si in the 1D profile). Moreover, for garnet, O – IF is also slightly higher at 50 pJ than at 30 pJ, yet the opposite is seen for spinel.

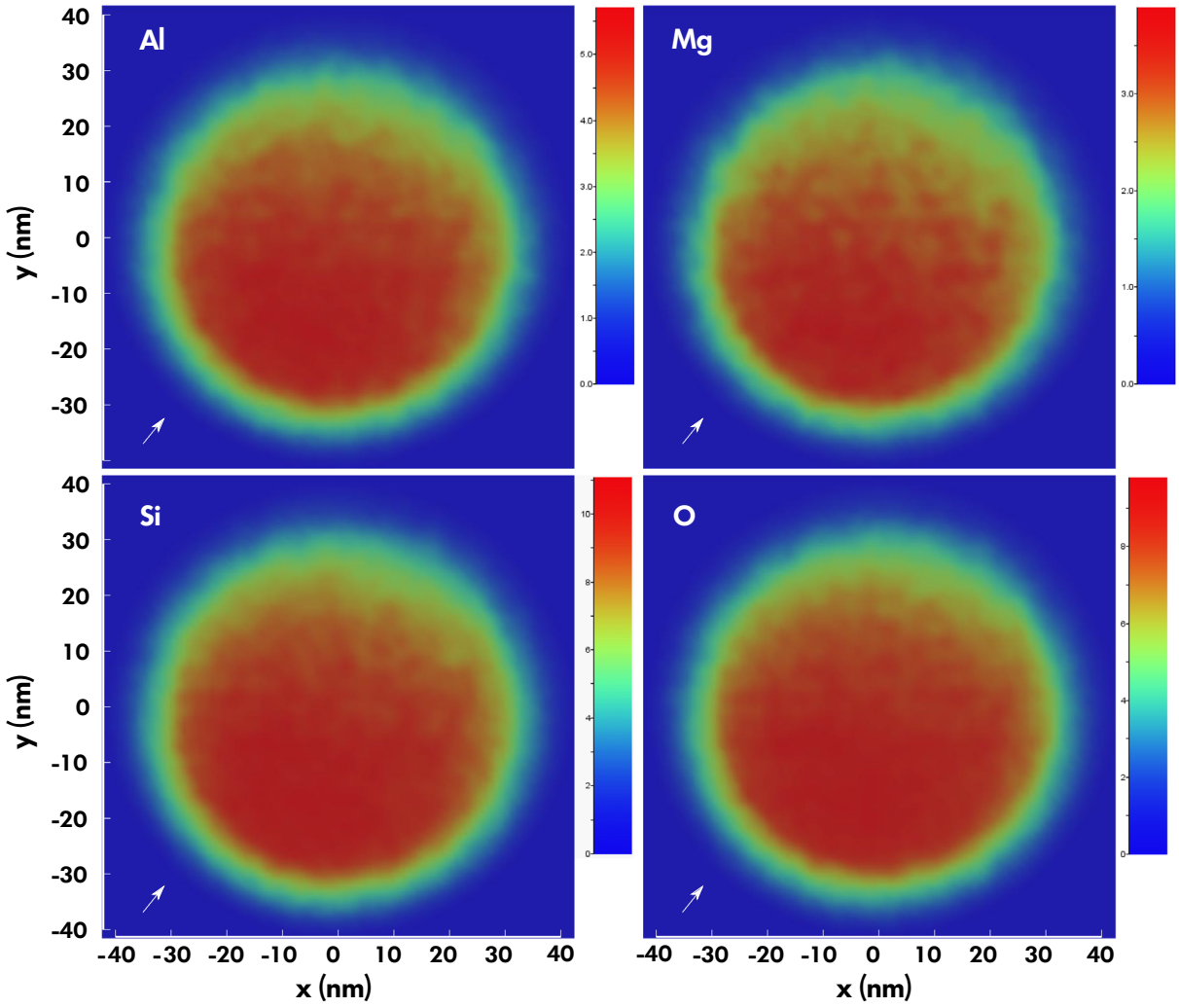

Figure 5. 2D ion density plots of garnet specimen analysed at 30 pJ (white arrows indicate laser beam direction).

Discussion

Spinel versus garnet laser interaction

A significant loss of oxygen was observed during APT analysis of spinel and garnet (Tables 1 and 2), except for the spinel specimen analysed at 50 pJ laser energy. This loss was greater in the case of the garnet with oxygen deficits as great as ~ 8.7 at% relative to the EPMA estimation (Table 3). Although electron spectroscopy studies demonstrated that the percentage of dication oxygen generated by O_2^+ ionisation is < 2% (Sigaud *et al.* 2013, Song *et al.* 2019), the influence of the user choice about the16 Da peak assignment on the underestimation of the oxygen concentration cannot be completely ruled out (see section 'Ion species' in Experimental procedures). Thus, atomic recount of representative data set for each mineral was performed, reassigning a specific percentage of the 16 Da peak counts to O_2^{2+} species (Table S3). Only for spinel, an 82% and 10% assignment of the 16 Da peak to dication oxygen compensates the oxygen deficit of respectively 30 and 50 pJ specimens. For garnet, even selecting the 16 Da peak as only O_2^{2+} (100% assignment), which represents an unlike scenario, oxygen is still below the nominal concentration (EPMA estimate). Mechanisms other than singly monoatomic and doubly diatomic species formation must then explain the recorded oxygen deficit.

The higher band gap and the lower thermal conductivity and diffusivity of garnet compared with spinel (Table 1) may be the reasons behind the lack of stoichiometry of the estimated garnet composition. The 2D density plots in Figures 4 and 5 show how the laser absorption varies between the two minerals. A typical unfavourable effect of the laser-assisted APT mode is the uneven tip heating due to the apex blunting on the laser-illuminated side (Morris *et al.*

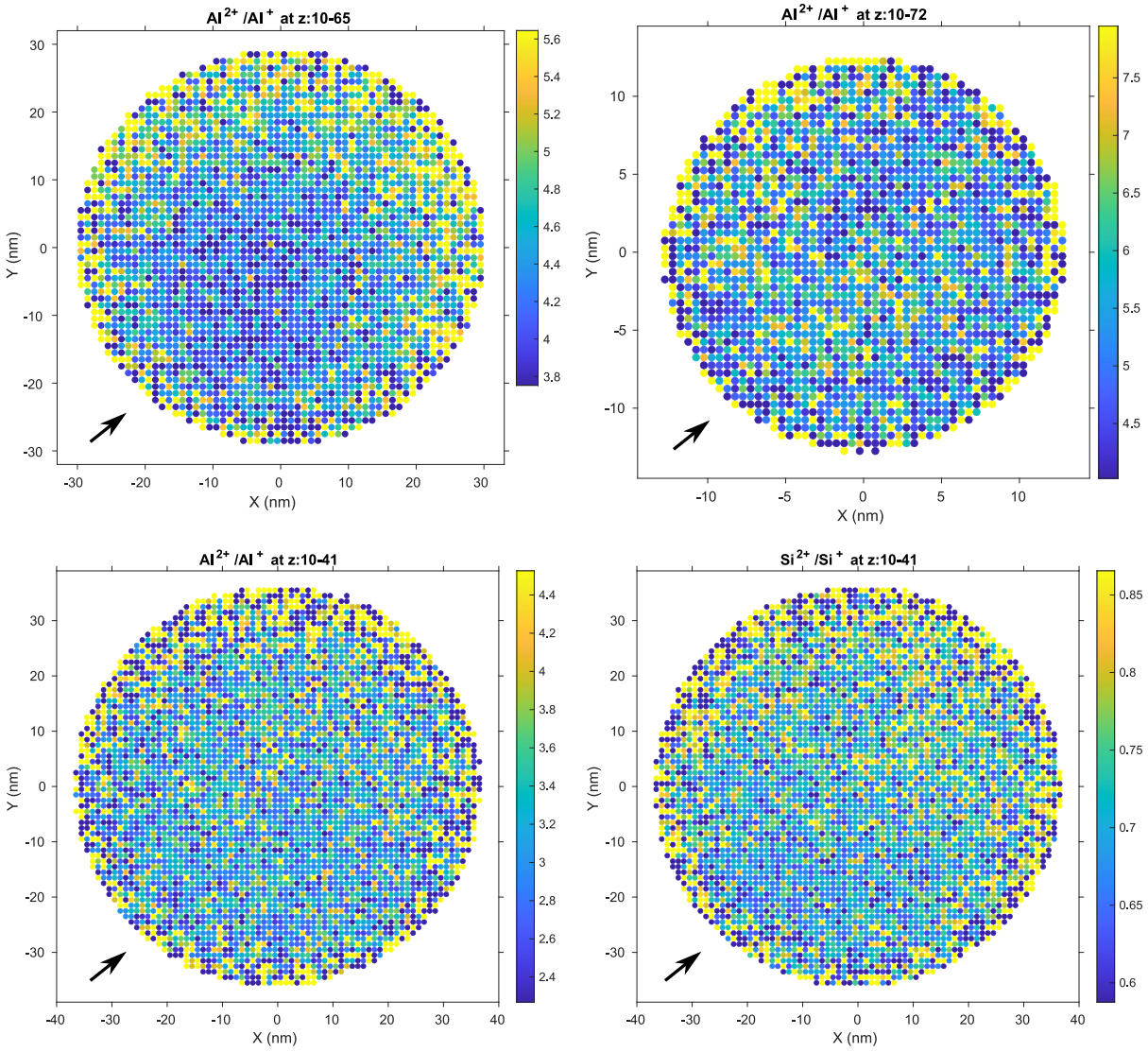

Figure 6. 2D maps of Al charge state ratio for spinel analysed at 30 pJ (top left) and 50 pJ (top right) laser pulse energy and Al (bottom left) and Si (bottom right) charge state ratios for garnet analysed at 30 pJ laser pulse energy. Each map is integrated over the tip length of the specimen. The black arrows indicate laser beam direction.

2019). This effect is more pronounced in materials with low laser penetration (or absorption) depth (δ) and low thermal diffusivity, which prevents a fast heat dissipation (Valderrama *et al.* 2015). The less uniform ion density distribution in garnet specimens, therefore, confirms the lower heat absorption capacity of this material. However, the specimen geometry (i.e., tip radius and shank angle) can also have a great influence on the laser absorption. As shown in section '2D ion density maps', smaller radius and shank angle seem to induce a decrease in the ion density gradient through the garnet specimen (Figure S6). This could be due to the tip diameter being more comparable to the laser absorption depth, which would cause a more uniform heating of the specimen surface. Still, a worse heat transfer is expected for garnet compared with spinel, independent of the initial tip shape and its evolution during analysis.

Spinel, on the other hand, exhibits a more symmetric ion density distribution (Figure 4), and the composition estimates at higher laser energy setting were in very good agreement with the EPMA results. In contrast with our observations, previous APT studies on MgO and CeO_2 stoichiometry found that low laser energy improved field ionisation due to the counter balancing increase of the applied voltage at constant evaporation rate, which led to higher electric field (Devaraj *et al.* 2013, Kirchhofer *et al.* 2013). However,

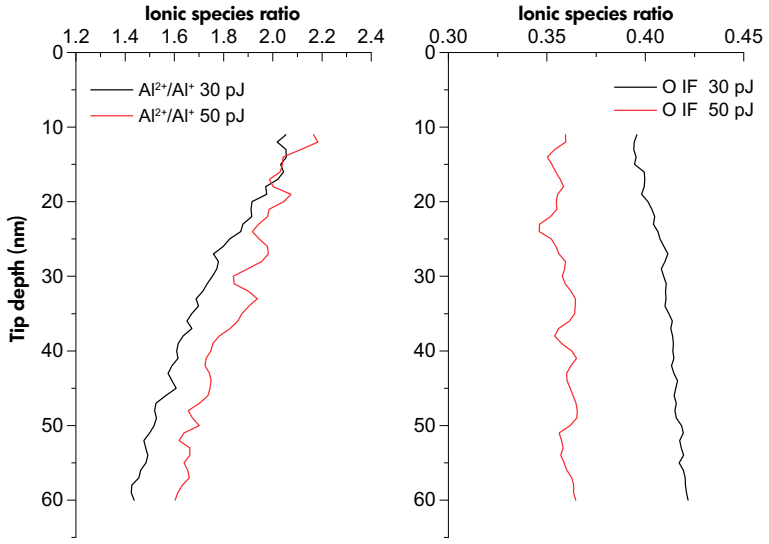

Figure 7. 1D profiles of Al charge state ratio (left) and oxygen fraction (right) for representative spinel specimens.

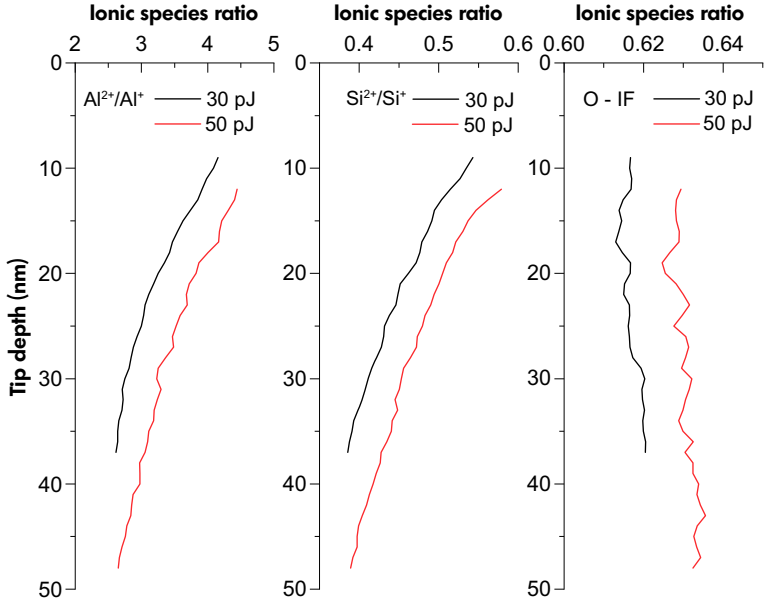

Figure 8. 1D profiles of, from left, Al and Si charge state ratio and oxygen fraction for representative garnet specimens.

Valderrama *et al.* (2015), in their study on UO_2, did report a small dependence of stoichiometry on the laser energy. This behaviour was ascribed to the higher thermal conductivity and diffusivity as well as the lower band gap energy of the U oxide with respect to Mg and Ce oxides. Although the different results obtained for spinel at 30 and 50 pJ laser energy support the existence of a laser effect on the recorded mineral stoichiometry, we cannot truly distinguish between the laser effect and the tip geometry effect on our spinel results. The radius (16 nm) and shank angle (9°) of the specimen analysed at 50 pJ laser energy are smaller than those of the specimens analysed at 30 pJ (24–36 nm radius; 19–29° shank angle). Because band structure and optical properties of dielectric materials, nominally absorption and extinction coefficients, can be altered by the intense voltage applied (Schreiber *et al.* 2014, Silaeva *et al.* 2014), a reliable estimation of the laser absorption depth for the specific APT laser wavelength (355 nm) and analysed

minerals is difficult to obtain. However, it is reasonable to assume that the smaller diameter of the spinel tip (run at 50 pJ) is probably comparable to the laser absorption depth that would lead to a more uniform heating of the tip surface. The disadvantage of a low radius and shank angle for a tip-shaped specimen is the worsened heat dissipation. Accordingly, at 50 pJ laser energy, larger thermal tails were observed as consequence of the poor heat dissipation. Hence, ion loss mechanisms (e.g., DC ion evaporation, surface ion diffusion) are expected.

Electric field intensity and distribution

The physical principle on which APT is based is the evaporation of atoms from a needle-shaped specimen induced by the application of a strong electric field (Kingham 1982). According to Equation (1), the rate of this thermally assisted process depends on the energy barrier that atoms have to overcome in order to be removed and ionised and is, hence, related to the surface electric field, which the barrier is a function of (Gault *et al.* 2012b, Larson *et al.* 2013). The exact value of the electric field at a specimen's surface during APT analysis, which cannot be measured directly, depends on the applied DC voltage and the tip shape. However, the charge state ratio has been proven to be a good indicator of the tip surface electric field (Mancini *et al.* 2014, Morris *et al.* 2018).

Overall, the 2D charge state ratio maps of spinel and garnet (Figure 6) indicate a variability of the electric field through the *x-y* plane that might reflect the presence of kink, adatoms or step-sites where the field normally enhances (Silaeva *et al.* 2013, Karahka and Kreuzer 2018). In addition, Equation (2) predicts that, at constant detection rate, the increase of the tip radius with *z* is compensated by the increasing applied voltage. This would maintain the same evaporation rate during the APT analysis but, as stated by Verberne *et al.* (2019), does not imply a constant electric field strength during the analysis, that is along the tip depth. In fact, Al and Si charge state ratios decrease with *z* (Figures 7 and 8), as a result of the continuous adjustment between the applied voltage, the radius and the *k* factor. This behaviour has previously been documented for the mineral rutile (Verberne *et al.* 2019).

Interestingly, higher CSR values were found for 50 pJ laser energy for the duration of the analysis for both spinel and garnet (Figures 7 and 8). This is in contrast with the post-ionisation theory (Kingham 1982) that predicts lower CSR (i.e., fewer double charged ions) for the decreasing electric field strength that is expected when laser energy is enhanced (Gault *et al.* 2010a). However, recent studies on rutile (Verberne *et al.* 2019) and magnetite (Schreiber *et al.* 2014) show a CSR-laser energy dependence that agrees with our findings. Schreiber *et al.* (2014) claimed that the Fe charge state fraction ($Fe^{2+}/(Fe^{+}+Fe^{2+})$) of magnetite depends on both laser energy and the electric field. In addition to the predicted post-ionisation process, direct evaporation of double ionised species would be favoured by higher laser energy. In the same study, the oxygen fraction was proven to be only field-dependent and hence was identified as a more reliable parameter describing the surface field. Accordingly, the O – IF should decrease with the laser energy enhancement, which is indeed what we observe in the case of spinel (Figure 7). However, the oxygen fraction of garnet specimens shows the opposite trend, perhaps reflecting a higher oxygen loss as neutral O_2 molecules for higher laser energy that would bias the relative concentration of single/double ions. In the same manner, higher O_2 loss, as the field decreases with the tip depth, could explain the slight apparent increase of the oxygen ion fraction in the z direction observed for both spinel and garnet (Figures 7 and 8).

Ion count loss mechanisms

Different causes have possibly induced a bias in the stoichiometry of the minerals analysed in the present study. The multihit event analysis undertaken for spinel and garnet has shed light on some of the main mechanisms that might have influenced atom loss during our APT runs (see Tables S1 and S2 for multihit % of each specimen). The main process linked to multihit events that is likely responsible for high count losses is the pile-up effect. When the same isotopes with identical charge state (e.g., two ions of $^{27}Al^{+}$) evaporate during multiple events, they may be under-counted if the evaporation occurs within the dead space–dead time window (Thuvander *et al.* 2013, Meisenkothen *et al.* 2015, Pedrazzini *et al.* 2017). The probability of pile-up occurring for a specific 'same isotope–same charge state' ion pair (M^n-M^n) would be correlated with its abundance, that is, the higher the ion pair counts the higher the pile-up effect (Peng *et al.* 2017). From the correlation histograms of spinel and garnet constructed in this study, quantification of M^n-M^n detected events was possible (Figure S11). The Al^{2+}-Al^{2+} pair is the most abundant in spinel followed by the O^{2+}-O^{2+} pair, which is more abundant in the specimen analysed at 30 pJ. In the case of garnet, the O^{+}-O^{+} pair is the most abundant, although substantial counts were also found for the O^{2+}-O^{2+} and Si^{+}-Si^{+} pairs. These results are consistent with the higher oxygen loss in garnet and would also explain the deficit of Al in the spinel composition estimate.

Other likely, although less significant, processes that are related to multiple events are late ion evaporation and molecular ion dissociation. In late evaporation, ions generated by this event would be recorded either as thermal tails of the main peaks or as background (for substantial delays). If there are delayed ion pairs (diagonals in Saxey plots), these ion counts can potentially be recovered from the overlapping peaks tails or the background where they would otherwise be hidden (Saxey 2011, Kruska and Schreiber 2015, Meisenkothen *et al.* 2015, Peng *et al.* 2018). However, the background of both spinel and garnet specimens was quite low (Tables S1 and S2) and does not seem to be related to the mineral stoichiometry misestimation, at least, not via the late evaporation mechanism. For garnet, a slightly lower background was recorded for specimens run at 50 pJ laser energy, but the inferred compositions did not differ. Also, larger thermal tails appeared in the spinel mass spectrum when higher laser energy was used, likely from slower cooling due to the tip shape (lower radius and shank angle). Nonetheless, our correlation histograms (Figure 3) show several diagonal lines for both minerals. Therefore, we cannot exclude the possibility that a small quantity of late evaporated ions is enclosed in the background and/or poorly deconvoluted peaks tails.

Molecular ion dissociation reactions (where molecules dissociate after evaporation from the specimen) have also been shown to occur in spinel and garnet during multihit events (see 'Multihit analysis' section). Daughter ions with significantly different mass-to-charge ratios from the parent species could be recognised as background, especially when late dissociations occur (Saxey 2011, Peng *et al.* 2018). However, previous works have shown that this mechanism does not significantly affect compositional estimates (Saxey 2011, Santhanagopalan *et al.* 2015). Nevertheless, dissociation reactions identified in this study demonstrate the possible formation of neutral species. Indeed, neutral oxygen molecules (O_2^0) likely formed through the pathway described by Equation 4g in the case of garnet (see online supporting information). Neutral molecule formation has been demonstrated to be a probable process leading to ion loss during APT analysis. Formation of neutral molecular oxygen during APT analysis has been proposed (Saxey 2011, Devaraj *et al.* 2013, Gault *et al.* 2016) and experimentally supported (Santhanagopalan *et al.* 2015). Also, migration of negative O ions down the shank of the tip-shaped specimen and its detachment as neutral molecules has been theorised (Karahka *et al.* 2015). It is likely that, especially during garnet analysis, neutral oxygen is registered as background or remains undetected, either because it does not reach the detector or because it does not have enough energy in relation to the detector efficiency (i.e., absence of signal amplification on the microchannel plate) (Gault *et al.* 2016).

A secondary mechanism of count loss (i.e., preferential evaporation) could also account for the underestimation of aluminium in the spinel composition. Atom evaporation between laser pulses may take place when the high applied voltage triggers the detachment of a species with lower zero-barrier evaporation field (electric field at which $Q_{EV}(F) \rightarrow 0$) compared with the surrounding species (Morris *et al.* 2018). This event is more likely to occur at low laser pulse energy and would increase the spectrum background (Kirchhofer *et al.* 2013, Mancini *et al.* 2014, Saxey *et al.* 2018). The slightly higher background recorded for spinel run at 30 pJ could thus be explained by atom preferential evaporation and would reflect a higher surface electric field.

Finally, the stoichiometric bias due to the different mechanisms of ion loss taking place during APT analysis itself may vary, as suggested by changes in ion density and charge state ratios, through the tip surface over the *x-y* plane and along the *z* direction. In some cases, a careful inspection of the changing atomic fractions with the tip length and/or width could be used to correct for biases in material stoichiometry (see, e.g., the results of Mancini *et al.* (2014) for APT analysis of GaN, AlN and ZnO). In this study, however, the variability of garnet and spinel composition with both specimen length and width was found to be minor (see Figure S12). Also, with the exception of spinel analysis at 50 pJ laser energy, a perfect match with the mineral stoichiometry inferred by EPMA was never obtained even for specific target areas that we would expect to contain the most reliable data.

Conclusions

A detailed evaluation of atom probe analysis on spinel and garnet samples was performed in order to shed light on how different minerals interact with the applied laser pulse and what processes may play a major role in biasing the stoichiometry measured by APT. In agreement with the theory, the spinel, with its lower band gap than garnet, displayed a better laser absorption when subjected to a high electric field and a bulk composition closer to that measured by EPMA. Still, a near stoichiometric composition was obtained only when higher laser pulse energy was used (50 pJ). Likewise, the garnet manifested a worse laser absorption with a stronger lateral effect (i.e., higher ion density on the laser-illuminated side), consistent with its slightly higher band gap and its lower thermal conductivity and diffusivity. Moreover, the APT-derived composition of garnet differed from the EPMA measurement in all cases.

The underestimation of oxygen content was the main issue, especially for garnet, and ion pile-up events and neutral molecule formation are considered the main mechanisms likely leading to atom count losses. However, other processes could partially account for the underestimation of the element concentrations in the analysed minerals, such as molecular ion species dissociation or the formation of oxygen dication. Such processes cannot be completely discarded even though their contribution is believed to be minimal.

Finally, this work highlights the dependence atom loss mechanisms have on the crystallochemistry and, more importantly, optical, thermal and electrical properties of the specific mineral in relation to the experimental parameters (i.e., laser energy). Together, these variables define the surface electric field that eventually controls the evaporation and ionisation of the atoms. It is likely that the electric field generated during APT analysis of garnet is not strong enough to promote sufficient 'metallisation' (i.e., band gap closure) on the specimens, causing uneven tip heating and possibly the formation of neutral molecules (e.g., O_2) that would not be ionised. As a result, a more reliable APT estimate of chemical composition is possible for spinel than for garnet.

Acknowledgements

This research was funded by the U.S. National Science Foundation (NSF), grant number EAR-1647012. The authors thank Dr. George E. Harlow (Dept. of Earth and Planetary Sciences, American Museum of Natural History) for providing the spinel sample and acknowledge the help of David Reinhard and Yimeng Chen, APT Product Manager and Applications Scientist, respectively, at CAMECA Instruments, Inc., for their support with the IVAS software data processing. Finally, this study utilised resources owned and maintained by the Alabama Analytical Research Center (AARC), supported by The University of Alabama. The authors have no conflicts of interest to declare.

Data availability statement

The data that support the findings of this study are available in the supplementary material of this article and from the corresponding author upon reasonable request.

References

Arey B.W., Perera D., Kovarik L., Qafoku O., Felmy A. and Gorman B. (2012)
Atom probe and TEM investigation of natural olivines. Microscopy and Microanalysis, 18, 658–659.

Bachhav M., Danoix F., Hannoyer B., Bassat J.M. and Danoix R. (2013)
Investigation of O-18 enriched hematite (α-Fe_2O_3) by laser assisted atom probe tomography. International Journal of Mass Spectrometry, 335, 57–60.

Bachhav M., Danoix R., Danoix F., Hannoyer B., Ogale S. and Vurpillot F. (2011a)
Investigation of wüstite (Fe1-xO) by femtosecond laser assisted atom probe tomography. Ultramicroscopy, 111, 584–588.

Bachhav M.N., Danoix R., Vurpillot F., Hannoyer B., Ogale S.B. and Danoix F. (2011b)
Evidence of lateral heat transfer during laser assisted atom probe tomography analysis of large band gap materials. Applied Physics Letters, 99, 084101.

Bachhav M., Dong Y., Skemer P. and Marquis E.A. (2015)
Atomic scale investigation of orthopyroxene and olivine grain boundaries by atom probe tomography. Microscopy and Microanalysis, 21, 1315–1316.

Bloch E.M., Jollands M.C., Gerstl S.S.A., Bouvier A.S., Plane F. and Baumgartner L.P. (2019)
Diffusion of calcium in forsterite and ultra-high resolution of experimental diffusion profiles in minerals using local electrode atom probe tomography. Geochimica et Cosmochimica Acta, 265, 85–95.

Branson O., Bonnin E.A., Perea D.E., Spero H.J., Zhu Z., Winters M., Hönisch B., Russell A.D., Fehrenbacher J.S. and Gagnon A.C. (2016)
Nanometer-scale chemistry of a calcite biomineralization template: Implications for skeletal composition and nucleation. Proceedings of the National Academy of Sciences of the United States of America, 113, 12934–12939.

Burns R.G. (1993)
Mineralogical applications of crystal field theory. Cambridge University Press (Cambridge).

Cappelli C. and Pérez-Huerta A. (2020)
Effect of crystallographic orientation on atom probe tomography geochemical data? Micron, 137, 102910.

Cerezo A., Smith G.D.W. and Clifton P.H. (2006)
Measurement of temperature rises in the femtosecond laser pulsed three-dimensional atom probe. Applied Physics Letters, 88, 154103.

Daly L., Lee M.R., Bagot P., Halpin J., Smith W., McFadzean S., O'Brien A.C., Griffin S., Hallis L.J. and Cohen B.E. (2020)
Exploring Mars at the nanoscale: Applications of transmission electron microscopy and atom probe tomography in planetary exploration. IOP Conference Series: Materials Science and Engineering, 891, 012008.

DeRocher K.A., Smeets P.J.M., Goodge B.H., Zachman M.J., Balachandran P.V., Stegbauer L., Cohen M.J., Gordon L.M., Rondinelli J.M., Kourkoutis L.F. and Joester D. (2020)
Chemical gradients in human enamel crystallites. Nature, 583, 66–71.

references

Devaraj A., Colby R., Hess W.P., Perea D.E. and Thevuthasan S. (2013)
Role of photoexcitation and field ionization in the measurement of accurate oxide stoichiometry by laser-assisted atom probe tomography. The Journal of Physical Chemistry Letters, 4, 993–998.

Devaraj A., Perea D.E., Liu J., Gordon L.M., Prosa T.J., Parikh P., Diercks D.R., Meher S., Kolli R.P., Meng Y.S. and Thevuthasan S. (2017)
Three-dimensional nanoscale characterisation of materials by atom probe tomography. International Materials Reviews, 63, 68–101.

Diercks D.R., Gorman B.P., Kirchhofer R., Sanford N., Bertness K. and Brubaker M. (2013)
Atom probe tomography evaporation behavior of C-axis GaN nanowires: Crystallographic, stoichiometric, and detection efficiency aspects. Journal of Applied Physics, 114, 184903.

Exertier F., La Fontaine A., Corcoran C., Piazolo S., Belousova E., Peng Z., Gault B., Saxey D.W., Fougerouse D., Reddy S.M., Pedrazzini S., Bagot P.A.J., Moody M.P., Langelier B., Moser D.E., Botton G.A., Vogel F., Thompson G.B., Blanchard P.T., Chiaramonti A.N., Reinhard D.A., Rice K.P., Schreiber D.K., Kruska K., Wang J. and Cairney J.M. (2018)
Atom probe tomography analysis of the reference zircon GJ-1: An interlaboratory study. Chemical Geology, 495, 27–35.

Felmy A.R., Qafoku O., Arey B.W., Kovarik L., Liu J., Perea D. and Ilton E.S. (2015)
Enhancing magnesite formation at low temperature and high CO_2 pressure: The impact of seed crystals and minor components. Chemical Geology, 395, 119–125.

Fougerouse D., Reddy S.M., Kirkland C.L., Saxey D.W., Rickard W.D. and Hough R.M. (2019)
Time-resolved, defect-hosted, trace element mobility in deformed Witwatersrand pyrite. Geoscience Frontiers, 10, 55–63.

Fougerouse D., Reddy S.M., Saxey D.W., Erickson T.M., Kirkland C.L., Rickard W.D.A., Seydoux-Guillaume A.M., Clark C. and Buick I.S. (2018)
Nanoscale distribution of Pb in monazite revealed by atom probe microscopy. Chemical Geology, 479, 251–258.

Fougerouse D., Reddy S.M., Saxey D.W., Rickard W.D.A., van Riessen A. and Micklethwaite S. (2016)
Nanoscale gold clusters in arsenopyrite controlled by growth rate not concentration: Evidence from atom probe microscopy. American Mineralogist, 101, 1916–1919.

Gault B., de Geuser F., Stephenson L.T., Moody M.P., Muddle B.C. and Ringer S.P. (2008)
Estimation of the reconstruction parameters for atom probe tomography. Microscopy and Microanalysis, 14, 296–305.

Gault B., La Fontaine A., Moody M.P., Ringer S.P. and Marquis E.A. (2010a)
Impact of laser pulsing on the reconstruction in an atom probe tomography. Ultramicroscopy, 110, 1215–1222.

Gault B., Moody M.P., Cairney J.M. and Ringer S.P. (2012a)
Atom probe microscopy. Springer-Verlag (New York), 396pp.

Gault B., Moody M.P., Cairney J.M. and Ringer S.P. (2012b)
Atom probe crystallography. Materials Today, 15, 378–386.

Gault B., Moody M.P., De Geuser F., La Fontaine A., Stephenson L.T., Haley D. and Ringer S.P. (2010b)
Spatial resolution in atom probe tomography. Microscopy and Microanalysis, 16, 99–110.

Gault B., Saxey D.W., Ashton M.W., Sinnott S.B., Chiaramonti A.N., Moody M.P. and Schreiber D.K. (2016)
Behavior of molecules and molecular ions near a field emitter. New Journal of Physics, 18, 033031.

Genareau K., Pérez-Huerta A. and Laiginhas F. (2019)
Atom probe tomography analysis of exsolved mineral phases. Journal of Visualized Experiments, 152, e59863.

Giesting P.A. and Hofmeister A.M. (2002)
Thermal conductivity of disordered garnets from infrared spectroscopy. Physical Review B, 65, 144305.

Gordon L.M., Cohen M.J., MacRenaris K.W., Pasteris J.D., Seda T. and Joester D. (2015)
Amorphous intergranular phases control the properties of rodent tooth enamel. Science, 347, 746–750.

Gordon L.M. and Joester D. (2011)
Nanoscale chemical tomography of buried organic–inorganic interfaces in the chiton tooth. Nature, 469, 194–197.

Gordon L.M., Tran L. and Joester D. (2012)
Atom probe tomography of apatites and bone-type mineralized tissues. ACS Nano, 6, 10667–10675.

Harris D., Johnson L., Seaver R., Lewis T., Turri G., Bass M., Zelmon D. and Haynes N. (2013)
Optical and thermal properties of spinel with revised (increased) absorption at 4 to 5 μm wavelengths and comparison with sapphire. Optical Engineering, 52, 087113.

Heck P.R., Stadermann F.J., Isheim D., Auciello O., Daulton T.L., Davis A.M., Elam J.W., Floss C., Hiller J., Larson D.J., Lewis J.B., Mane A., Pellin M.J., Savina M.R., Seidman D.N. and Stephan T. (2014)
Atom-probe analyses of nanodiamonds from Allende. Meteoritics and Planetary Science, 49, 453–467.

Karahka M. and Kreuzer H.J. (2013)
Field evaporation of oxides: A theoretical study. Ultramicroscopy, 132, 54–59.

references

Karahka M. and Kreuzer H.J. (2015)
Field evaporation of insulators and semiconductors: Theoretical insights for ZnO. Ultramicroscopy, 159, 156–161.

Karahka M. and Kreuzer H.J. (2018)
Kinetics of silicon field evaporation. Materials Characterization, 146, 319–323.

Karahka M., Xia Y. and Kreuzer H.J. (2015)
The mystery of missing species in atom probe tomography of composite materials. Applied Physics Letters, 107, 062105.

Kelly T.F., Vella A., Bunton J.H., Houard J., Silaeva E.P., Bogdanowicz J. and Vandervorst W. (2014)
Laser pulsing of field evaporation in atom probe tomography. Current Opinion in Solid State and Materials Science, 18, 81–89.

Kingham D.R. (1982)
The post-ionization of field evaporated ions: A theoretical explanation of multiple charge states. Surface Science, 116, 273–301.

Kinno T., Tomita M., Ohkubo T., Takeno S. and Hono K. (2014)
Laser-assisted atom probe tomography of ^{18}O-enriched oxide thin film for quantitative analysis of oxygen. Applied Surface Science, 290, 194–198.

Kirchhofer R., Teague M.C. and Gorman B.P. (2013)
Thermal effects on mass and spatial resolution during laser pulse atom probe tomography of cerium oxide. Journal of Nuclear Materials, 436, 23–28.

Kruska K. and Schreiber D.K. (2015)
Background recovery through the quantification of delayed evaporation multi-ion events in atom-probe data. Microscopy and Microanalysis, 21, 857–858.

Kuhlman K.R., Martens R.L., Kelly T.F., Evans N.D. and Miller M.K. (2001)
Fabrication of specimens of metamorphic magnetite crystals for field ion microscopy and atom probe microanalysis. Ultramicroscopy, 89, 169–176.

La Fontaine A., Piazolo S., Trimby P., Yang L. and Cairney J.M. (2017)
Laser-assisted atom probe tomography of deformed minerals: A zircon case study. Microscopy and Microanalysis, 23, 404–413.

La Fontaine A., Zavgorodniy A., Liu H., Zheng R., Swain M. and Cairney J. (2016)
Atomic-scale compositional mapping reveals Mg-rich amorphous calcium phosphate in human dental enamel. Science Advances, 2, e1601145.

Larson D.J., Prosa T., Ulfig R.M., Geiser B.P. and Kelly T.F.J. (2013)
Local electrode atom probe tomography. Springer-Verlag (New York), 318pp.

Lefebvre-Ulrikson W., Vurpillot F. and Sauvage X. (2016)
Atom probe tomography: Put theory into practice. Academic Press (London), 416pp.

Lewis J.B., Floss C., Isheim D., Daulton T.L., Seidman D.N. and Ogliore R. (2020)
Origins of meteoritic nanodiamonds investigated by coordinated atom-probe tomography and transmission electron microscopy studies. Meteoritics and Planetary Science, 55, 1382–1403.

Mancini L., Amirifar N., Shinde D., Blum I., Gilbert M., Vella A., Vurpillot F., Lefebvre W., Lardé R., Talbot E., Pareige P., Portier X., Ziani A., Davesnne C., Durand C., Eymery J., Butté R., Carlin J.-F., Grandjean N. and Rigutti L. (2014)
Composition of wide bandgap semiconductor materials and nanostructures measured by atom probe tomography and its dependence on the surface electric field. The Journal of Physical Chemistry C, 118, 24136–24151.

McMurray S., Gorman B. and Diercks D. (2011)
TEM and atom probe investigation of calcium carbonate precipitation in seawater. Microscopy and Microanalysis, 17, 758–759.

Meisenkothen F., Steel E.B., Prosa T.J., Henry K.T. and Prakash K.R. (2015)
Effects of detector dead-time on quantitative analyses involving boron and multi-hit detection events in atom probe tomography. Ultramicroscopy, 159, 101–111.

Miller M.K. and Forbes R.G. (2014)
The art of specimen preparation. In: Miller M.K. and Forbes R.G. (eds), Atom-probe tomography: The local electrode atom probe. Springer US (Boston, MA), 189–228.

Miller M.K., Russell K.F., Thompson K., Alvis R. and Larson D.J. (2007)
Review of atom probe FIB-based specimen preparation methods. Microscopy and Microanalysis, 13, 428–436.

Morris J.H.R., Cuduvally R., Melkonyan D., Fleischmann C., Zhao M., Arnoldi L., van der Heide P. and Vandervorst W. (2018)
Toward accurate composition analysis of GaN and AlGaN using atom probe tomography. Journal of Vacuum Science and Technology B, 36, 03F1301–03F1306.

Morris J.H.R., Cuduvally R., Melkonyan D., Zhao M., van der Heide P. and Vandervorst W. (2019)
Atom probe of GaN/AlGaN heterostructures: The role of electric field, sample crystallography and laser excitation on quantification. Ultramicroscopy, 206, 112813.

Müller M., Smith G.D.W., Gault B. and Grovenor C.R.M. (2012)
Compositional nonuniformities in pulsed laser atom probe tomography analysis of compound semiconductors. Journal of Applied Physics, 111, 064908.

Nitsan U. and Shankland T.J. (1976)
Optical properties and electronic structure of mantle silicates. Geophysical Journal International, 45, 59–87.

Pedrazzini S., London A.J., Gault B., Saxey D., Speller S., Grovenor C.R.M., Danaie M., Moody M.P., Edmondson P.D. and Bagot P.A.J. (2017)
Nanoscale stoichiometric analysis of a high-temperature superconductor by atom probe tomography. Microscopy and Microanalysis, 23, 414–424.

references

Peng Z., Gault B., Raabe D., Ashton M.W., Sinnott S.B., Choi P.-P. and Li Y. (2017)
On the multiple event detection in atom probe tomography. Microscopy and Microanalysis, 23, 618–619.

Peng Z., Vurpillot F., Choi P.P., Li Y., Raabe D. and Gault B. (2018)
On the detection of multiple events in atom probe tomography. Ultramicroscopy, 189, 54–60.

Pérez-Huerta A. and Laiginhas F. (2018)
Preliminary data on the nanoscale chemical characterization of the inter-crystalline organic matrix of a calcium carbonate biomineral. Minerals, 8, 223.

Pérez-Huerta A., Laiginhas F., Reinhard D.A., Prosa T.J. and Martens R.L. (2016)
Atom probe tomography (APT) of carbonate minerals. Micron, 80, 83–89.

Pérez-Huerta A., Suzuki M., Cappelli C., Laiginhas F. and Kintsu H. (2019)
Atom probe tomography (APT) characterization of organics occluded in single calcite crystals: Implications for biomineralization studies. C — Journal of Carbon Research, 5, 50.

Pérez-Huerta A., Walker S.E. and Cappelli C. (2020)
In situ geochemical analysis of organics in growth lines of antarctic scallop shells: Implications for sclerochronology. Minerals, 10, 529.

Peterman E.M., Reddy S.M., Saxey D.W., Fougerouse D., Snoeyenbos D.R. and Rickard W.D.A. (2019)
Nanoscale processes of trace element mobility in metamorphosed zircon. Contributions to Mineralogy and Petrology, 174, 92.

Piazolo S., Belousova E., La Fontaine A., Corcoran C. and Cairney J.M. (2017)
Trace element homogeneity from micron- to atomic scale: Implication for the suitability of the zircon GJ-1 as a trace element reference material. Chemical Geology, 456, 10–18.

Reddy S.M., Saxey D.W., Rickard W.D.A., Fougerouse D., Montalvo S.D., Verberne R. and van Riessen A. (2020)
Atom probe tomography: Development and application to the geosciences. Geostandards and Geoanalytical Research, 44, 5–50.

Riley J.R., Bernal R.A., Li Q., Espinosa H.D., Wang G.T. and Lauhon L.J. (2012)
Atom probe tomography of *a*-axis GaN nanowires: Analysis of nonstoichiometric evaporation behavior. ACS Nano, 6, 3898–3906.

Santhanagopalan D., Schreiber D.K., Perea D.E., Martens R.L., Janssen Y., Khalifah P. and Meng Y.S. (2015)
Effects of laser energy and wavelength on the analysis of $LiFePO_4$ using laser assisted atom probe tomography. Ultramicroscopy, 148, 57–66.

Saxey D.W. (2011)
Correlated ion analysis and the interpretation of atom probe mass spectra. Ultramicroscopy, 111, 473–479.

Saxey D.W., Reddy S.M., Fougerouse D. and Rickard W.D.A. (2018)
The optimization of zircon analyses by laser-assisted atom probe microscopy. In: Moser D.E., Corfu F., Darling J.R., Reddy S.M. and Tait K. (eds), Microstructural Geochronology. Wiley (Hoboken, NJ, USA), 293–313.

Schreiber D.K., Chiaramonti A.N., Gordon L.M. and Kruska K. (2014)
Applicability of post-ionization theory to laser-assisted field evaporation of magnetite. Applied Physics Letters, 105, 244106.

Shengli J., Tiecheng L., Yao L. and Jun C. (2012)
Ab initio many-body study of the electronic and optical properties of $MgAl_2O_4$ spinel. Journal of Applied Physics, 111, 043516.

Sigaud L., Ferreira N. and Montenegro E.C. (2013)
Absolute cross sections for O_2 dication production by electron impact. The Journal of Chemical Physics, 139, 024302.

Silaeva E.P., Arnoldi L., Karahka M.L., Deconihout B., Menand A., Kreuzer H.J. and Vella A. (2014)
Do dielectric nanostructures turn metallic in high-electric dc fields? Nano Letters, 14, 6066–6072.

Silaeva E.P., Houard J., Hideur A., Martel G. and Vella A. (2015)
Field evaporation of semiconductors assisted by nonequilibrium phonon excitations. Physical Review B, 92, 195307.

Silaeva E.P., Karahka M. and Kreuzer H.J. (2013)
Atom probe tomography and field evaporation of insulators and semiconductors: Theoretical issues. Current Opinion in Solid State and Materials Science, 17, 211–216.

Song S., Ding B., Xu W., Nicolas C., Patanen M., Nandi S., Bozek J., Miron C., Xiao Z. and Liu X.-J. (2019)
Sequential electron emission and nuclear dissociation after the O 1s → (4- υ)4pσ excitation in O_2 molecules. Physical Review A, 99, 022511.

Taylor S.D., Liu J., Zhang X., Arey B.W., Kovarik L., Schreiber D.K., Perea D.E. and Rosso K.M. (2019)
Visualizing the iron atom exchange front in the Fe(II)-catalyzed recrystallization of goethite by atom probe tomography. Proceedings of the National Academy of Sciences of the United States of America, 116, 2866–2874.

Thuvander M., Kvist A., Johnson L.J.S., Weidow J. and Andrén H.-O. (2013)
Reduction of multiple hits in atom probe tomography. Ultramicroscopy, 132, 81–85.

references

Valderrama B., Henderson H.B., Yablinsky C.A., Gan J., Allen T.R. and Manuel M.V. (2015)
Investigation of material property influenced stoichiometric deviations as evidenced during UV laser-assisted atom probe tomography in fluorite oxides. Nuclear Instruments and Methods in Physics Research Section B, 359, 107–114.

Valley J.W., Cavosie A.J., Ushikubo T., Reinhard D.A., Lawrence D.F., Larson D.J., Clifton P.H., Kelly T.F., Wilde S.A., Moser D.E. and Spicuzza M.J. (2014)
Hadean age for a post-magma-ocean zircon confirmed by atom-probe tomography. Nature Geoscience, 7, 219.

Valley J.W., Reinhard D.A., Cavosie A.J., Ushikubo T., Lawrence D.F., Larson D.J., Kelly T.F., Snoeyenbos D.R. and Strickland A. (2015)
Nano- and micro-geochronology in Hadean and Archean zircons by atom-probe tomography and SIMS: New tools for old minerals. American Mineralogist, 100, 1355–1377.

Vella A., Mazumder B., Da Costa G. and Deconihout B. (2011)
Field evaporation mechanism of bulk oxides under ultra fast laser illumination. Journal of Applied Physics, 110, 044321.

Verberne R., Reddy S.M., Saxey D.W., Fougerouse D., Rickard W.D.A., Plavsa D., Agangi A. and Kylander-Clark A.R.C. (2020)
The geochemical and geochronological implications of nanoscale trace-element clusters in rutile. Geology, 48, 1126–1130.

Verberne R., Saxey D.W., Reddy S.M., Rickard W.D.A., Fougerouse D. and Clark C. (2019)
Analysis of natural rutile (TiO_2) by laser-assisted atom probe tomography. Microscopy and Microanalysis, 25, 539–546.

Vurpillot F. (2016)
Field ion emission mechanisms. In: Lefebvre-Ulrikson W., Vurpillot F. and Sauvage X. (eds), Atom probe tomography. Academic Press (London), 17–72.

Vurpillot F., Houard J., Vella A. and Deconihout B. (2009)
Thermal response of a field emitter subjected to ultra-fast laser illumination. Journal of Physics D, 42, 125502.

Vurpillot F. and Oberdorfer C. (2015)
Modeling atom probe tomography: A review. Ultramicroscopy, 159, 202–216.

Weber J., Barthel J., Brandt F., Klinkenberg M., Breuer U., Kruth M. and Bosbach D. (2016)
Nano-structural features of barite crystals observed by electron microscopy and atom probe tomography. Chemical Geology, 424, 51–59.

Weber J., Bracco J.N., Poplawsky J.D., Ievlev A.V., More K.L., Lorenz M., Bertagni A.L., Jindra S.A., Starchenko V., Higgins S.R. and Stack A.G. (2018)
Unraveling the effects of strontium incorporation on barite growth – *In situ* and *ex situ* observations using multiscale chemical imaging. Crystal Growth and Design, 18, 5521–5533.

White L.F., Kizovski T.V., Tait K.T., Langelier B., Gordon L.M., Harlov D. and Norberg N. (2018)
Nanoscale chemical characterisation of phase separation, solid state transformation, and recrystallization in feldspar and maskelynite using atom probe tomography. Contributions to Mineralogy and Petrology, 173, 87.

Xia Y., Karahka M. and Kreuzer H.J. (2015)
Field evaporation of ZnO: A first-principles study. Journal of Applied Physics, 118, 025901.

Supporting information

The following supporting information may be found in the online version of this article:

Figure S1. Scanning electron microscopy images of representative tip specimens of spinel (a, b) and garnet (c, d).

Figure S2. 3D reconstruction of representative tip specimen for spinel (top) and garnet (bottom).

Figure S3. 3D reconstruction of specimen 4184-M19 run at 50 pJ laser energy.

Table S1. Instrument settings and input and output experimental parameters for spinel and garnet at 30 pJ laser pulse energy.

Table S2. Instrument settings and input and output experimental parameters for spinel and garnet at 50 pJ laser pulse energy.

Table S3. APT composition estimates of representative spinel and garnet specimens calculated assigning different percentage of the 16 Da peak to O_2^{2+} species.

This material is available from: http://onlinelibrary.wiley.com/doi/10.1111/ggr.12395/abstract (This link will take you to the article abstract).